

A silicon source of heralded single photons at 2 μm ^{EP}

Cite as: APL Photonics 6, 126103 (2021); <https://doi.org/10.1063/5.0063393>

Submitted: 14 July 2021 • Accepted: 22 November 2021 • Published Online: 07 December 2021

 S. Signorini,  M. Sanna, S. Piccione, et al.

COLLECTIONS

 This paper was selected as an Editor's Pick



View Online



Export Citation

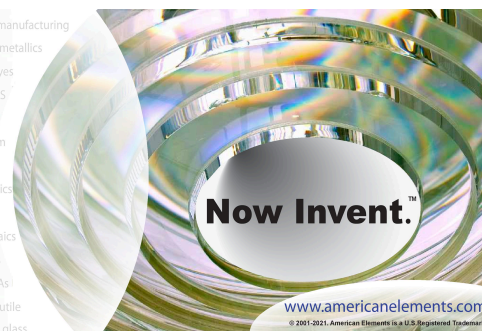


CrossMark



yttrium iron garnet glassy carbon beamsplitters fused quartz additive manufacturing
zeolites III-IV semiconductors gallium lump copper nanoparticles organometallics
nano ribbons barium fluoride europium phosphors photonics infrared dyes
epitaxial crystal growth ultra high purity materials transparent ceramics CIGS
cerium oxide polishing powder surface functionalized nanoparticles MBE grade materials thin film
silver nanoparticles perovskites MOCVD beta-barium borate rare earth metals quantum dots
osmium scintillation Ce:YAG refractory metals laser crystals anode lithium niobate InAs wafers
dysprosium pellets MOFs AuNPs chalogenides ZnS CdTe perovskite crystals transparent ceramics

The Next Generation of Material Science Catalogs




A silicon source of heralded single photons at $2\ \mu\text{m}$

Cite as: APL Photon. 6, 126103 (2021); doi: 10.1063/5.0063393

Submitted: 14 July 2021 • Accepted: 22 November 2021 •

Published Online: 7 December 2021



S. Signorini,^{1,a)}  M. Sanna,¹  S. Piccione,¹ M. Ghulinyan,²  P. Tidemand-Lichtenberg,³  C. Pedersen,³ 
and L. Pavesi¹ 

AFFILIATIONS

¹Nanoscience Laboratory, Department of Physics, University of Trento, Via Sommarive 14, 38123 Trento, Italy

²Centre for Sensors and Devices, Fondazione Bruno Kessler, Via Sommarive 18, 38123 Trento, Italy

³Department of Photonics Engineering, DTU Fotonik, Technical University of Denmark, Roskilde 4000, Denmark

^{a)} Author to whom correspondence should be addressed: stefano.signorini-1@unitn.it

ABSTRACT

Mid-infrared integrated quantum photonics is a promising platform for applications in sensing and metrology. However, there are only a few examples of on-chip single-photon sources at these wavelengths. These have limited performances with respect to their C-band counterparts. In this work, we demonstrate a new approach to generate heralded single photons in the mid-infrared on a silicon chip. By using a standard C-band pump, the inter-modal spontaneous four-wave mixing enables the generation of the herald idler at 1259.7 nm and the heralded signal at 2015 nm. The idler photon is easily detected with a common infrared single-photon detector while the signal photon is upconverted to visible before its detection. In this way, we are able to operate a mid-infrared source without the need for mid-infrared detectors and laser sources. By measuring a heralded $g^{(2)}$ of 0.23 ± 0.08 , we demonstrate the single-photon behavior of the source as well as the feasibility of multi-photon coincidence measurements beyond $2\ \mu\text{m}$ with our setup. The source exhibits a high-intrinsic heralding efficiency of $(59 \pm 5)\%$, a maximum coincidence to accidental ratio of 40.4 ± 0.9 , and a generation probability of $(0.70 \pm 0.10)\ \text{W}^{-2}$.

© 2021 Author(s). All article content, except where otherwise noted, is licensed under a Creative Commons Attribution (CC BY) license (<http://creativecommons.org/licenses/by/4.0/>). <https://doi.org/10.1063/5.0063393>

1. INTRODUCTION

Mid-infrared (MIR) light ($2\text{--}15\ \mu\text{m}$) is of importance in a wide range of technological applications. Free space telecommunication,¹ LIDAR,² environmental monitoring,³ medicine, and biology^{4–7} are only a few of the several fields where MIR optics plays a role. In particular, gas sensing exploits the strong absorption bands in the MIR⁸ to enhance remarkably the sensitivity of absorption spectroscopy measurements.^{9–11} Despite the great interest in developing MIR applications, these are still hindered by immature optical MIR devices. Quantum optics offers new solutions to mitigate such limitations. Sub-Poissonian light can be used to beat the shot-noise limit.^{12,13} Entangled photons have been used to demonstrate new imaging and spectroscopy techniques that are able to get rid of detection technology limitations, namely, ghost imaging^{14,15} or an undetected photon measurement.^{16–18} To enable quantum-enhanced MIR metrology leveraging these quantum-based measurement strategies, a source of single or entangled photons beyond $2\ \mu\text{m}$ is required. Up until now, these techniques have been investigated

only with bulky, alignment tolerant, and expensive instrumentation based on free space nonlinear crystals.^{17,19} To develop feasible, robust, and affordable quantum technologies, miniaturization and cost-effectiveness are crucial. Such requirements can be met by means of integrated photonics. In particular, silicon photonics integrated circuits are characterized by mature CMOS (complementary metal–oxide–semiconductor) fabrication technology, which allows for robust, stable, low power consumption and efficient light manipulation at the chip scale.²⁰ On-chip MIR quantum measurements would enable efficient and cost-effective sensors, boosting the development of MIR and quantum technologies. Recently, an on-chip silicon-on-insulator (SOI) source of MIR pairs has been reported.²¹ However, in this work, a pump in the MIR is used, and both the paired photons are beyond $2\ \mu\text{m}$, thus, requiring specific MIR technologies for both the pump and the detection. Recently, we demonstrated that inter-modal spontaneous four-wave mixing (SFWM) can be used in silicon waveguides to generate correlated pairs with one photon in the near-infrared (NIR) and the other in the MIR by using a standard C-band pump.^{22,23} However, we never detected

the MIR correlated photon. Instead, we inferred its existence by measuring the high-energy photon in the pair.

In this work, we demonstrate a SOI waveguide source of heralded MIR single photons based on inter-modal SFWM, performing the MIR detection by means of an upconversion system.²⁴ The herald photon lays in the NIR, where it can be efficiently detected with traditional InGaAs single-photon avalanche photodiodes (SPADs). Moreover, the photons are generated in discrete bands, thus, removing the need for narrowband filters to select the operating wavelengths of the signal and idler.²⁵ As a result, the heralding efficiency is increased with respect to traditional intra-modal SFWM, as witnessed by the measured intrinsic heralding efficiency $\eta_I = 59(5)\%$. The large detuning of the generated photons is also beneficial for the pump and Raman noise rejection that can be easily removed with broadband filters. The pump is a standard 1550 nm pulsed laser. Therefore, we do not require MIR technologies to operate a source beyond 2 μm . We assessed the single-photon behavior of the source by measuring a heralded $g_h^{(2)}(0)$ of 0.23(8). We monitored the idler–signal coincidences, reporting a maximum coincidence to accidental ratio of 40.4(9), exceeding the performance of current integrated sources of MIR heralded photons.²¹

This paper is organized as follows: In Sec. II, we describe the chip design and the experimental setup. In Sec. III, our approach to data analysis is extensively described. In Sec. IV, the results relative to the source characterization are reported. Section V concludes this paper.

II. CHIP DESIGN AND EXPERIMENTAL SETUP

Conventional intra-modal SFWM involves only one waveguide mode in the conversion of two input pump photons into an idler photon and a signal photon. On the contrary, inter-modal SFWM leverages the different chromatic dispersions of different optical spatial modes of a photonic waveguide to achieve phase matching.²² Different modal combinations are possible, depending on the waveguide cross section, which also determines the generated signal and idler wavelengths. In this work, we use the transverse electric (TE), fundamental (TE0), and first (TE1) waveguide modes in a rib SOI waveguide. The waveguide has a width of 1.95 μm and a height of 0.190 μm over a 0.3 μm thick slab. The waveguide length is 1.5 cm. The waveguide and the slab are in silicon, while the top and bottom claddings are in silica. The simulated intensity profiles of the TE0 and TE1 modes are shown in Fig. 1(a).

The inter-modal combination used in our work involves the pump on both the TE0 and TE1, the idler on the TE0, and the signal on the TE1. A peculiar advantage of intermodal SFWM is the generation of the signal and idler photons on different waveguide modes. In this way, the idler and signal can be easily separated with high efficiency through an on-chip mode converter. The experimental setup is detailed in Fig. 1(b). The upconverter (UC) is constituted by a continuous wave (CW) laser cavity, where a Nd:YVO₄ pumped intra-cavity periodically poled lithium niobate (PPLN) allows for sum-frequency generation (SFG) between the intra-cavity laser (1064 nm) and the input MIR photons. We used a PPLN from HC

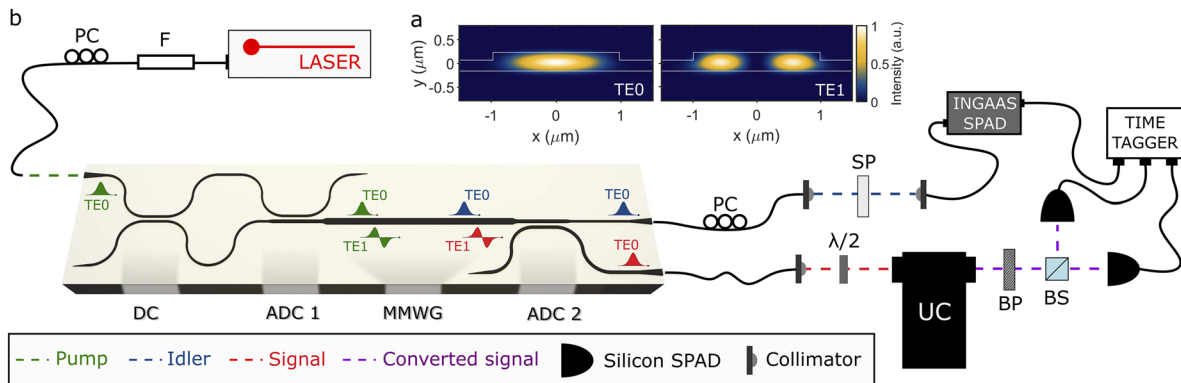


FIG. 1. (a) Simulated intensity profiles of the TE0 and TE1 spatial modes in the multimode waveguide. (b) Experimental setup used in the experiment. For the pump (green), we used a pulsed laser at 1550.3 nm (40 ps pulse width, 80 MHz repetition rate), which, after passing through a bandpass filter (F) and a polarization controller (PC), is coupled to the chip via a tapered lensed fiber. The chip schematics are shown in the bottom part. On the chip, after a 3-dB directional coupler (DC), half of the pump remains on the TE0, while the other half is converted to the TE1 via an asymmetric directional coupler (ADC1) (92% efficiency). In this way, the pump reaches the multimode waveguide (MMWG) equally splitted on the TE0 and TE1 modes. In the MMWG, the inter-modal SFWM process generates the idler (blue) and signal (red) photons in the TE0 and TE1 modes, respectively. The signal is then converted to the TE0 via another asymmetric directional coupler (ADC2). In this way, the idler and signal can be easily separated on the chip. The idler and signal are then out-coupled from the chip via two tapered lensed fibers. Pump residual and Raman noise are rejected from the idler beam by means of a short pass filter (SP) with a cut-off wavelength of 1335 nm. The idler is then detected via an InGaAs SPAD (ID Quantique IDQ210), triggered by the pump with a gate width of 1.90 ns. The signal, after being out-coupled from the chip, is polarization rotated through a free space half-wave plate ($\lambda/2$) and upconverted to the visible through an upconverter (UC) system. The UC system includes a long pass filter with a cut-on wavelength of 1900 nm, which rejects the C-band pump. The UC introduces noise photons collinear to the upconverted signal and centered at the same wavelength. A bandpass filter (BP) is used to filter away part of this noise, without filtering the upconverted signal (purple). Then, the signal photons are analyzed by means of a Hanbury Brown and Twiss (HBT) interferometer. The HBT interferometer is composed of a 50/50 beam splitter (BS) with two visible silicon SPADs (Excelitas SPCM-AQRH-12) monitoring the BS reflection and transmission ports. The visible SPADs are used in free-running mode. A time tagging unit (Swabian Time Tagger 20) is used to monitor individual singles and coincidences between the three detectors.

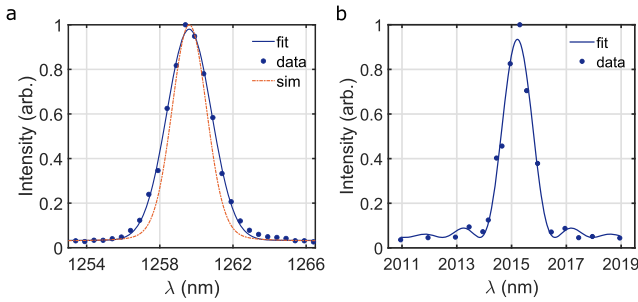


FIG. 2. (a) Measured intensity spectrum of the idler beam. The fit has been made with a Gaussian function, showing a FWHM of 2.87 ± 0.07 nm. This measurement is affected by the transfer function of the monochromator used to perform the measurement, which enlarges the actual bandwidth of the generation. We simulated the idler spectrum considering also the widening due to the monochromator (orange dashed line). To evaluate the actual bandwidth of the idler (2.0 ± 0.3 nm), we deconvolved the response function of the monochromator. (b) Measured spectral response of the upconverter. The response has been fitted by a squared sinc function, as expected for a sum-frequency generation process. The FWHM is 1.15 ± 0.12 nm.

Photonics with a length of 25 mm, tuned in temperature to upconvert the MIR signal at 2015 nm to the visible at 696 nm. The UC used is the same as that used in the work of Mancinelli *et al.*,²⁴ though tuned at the wavelengths of interest here. The transfer function of the UC is reported in Fig. 2(b), showing a full width at half maximum (FWHM) of 1.15 ± 0.12 nm. We used a pump pulsed laser centered at 1550.30 ± 0.05 nm with 40 ps pulse width and 80 MHz repetition rate. The generated idler spectrum is reported in Fig. 2. We measured a discrete band centered at 1259.7 ± 0.5 nm with a FWHM of 2.0 ± 0.3 nm. The measured FWHM of the idler is compatible with the simulated one of 1.81 nm, as shown in Fig. 2(a). According to the energy conservation, the signal is generated at 2015.2 ± 1.5 nm. From the measured idler bandwidth, we estimated a FWHM of 5.1 ± 0.8 nm for the signal. Therefore, the UC filters the signal photons according to the spectrum shown in Fig. 2(b).

III. DATA ANALYSIS

With SFWM, the detection probabilities per pulse for the idler (p_i), signal (p_s), coincidences (p_{si}), and accidentals (p_{acc}) are quadratic with the pump power P . In the limit of low transmission efficiencies for the signal and idler,²⁶ they can be written as

$$p_i = \xi P^2 \eta_i + d_i, \quad (1a)$$

$$p_s = \xi P^2 \eta_s + d_s, \quad (1b)$$

$$p_{si} = \xi P^2 \eta_i \eta_s, \quad (1c)$$

$$p_{acc} = p_i p_s, \quad (1d)$$

where ξ is the generation probability per pulse per squared unit power;²¹ η_i and η_s are the total transmission efficiencies for the idler and signal channels (from generation to detection), respectively; and d_i and d_s are the dark count probabilities per pulse for the idler and signal channels, respectively. Equation (1c) refers to net coincidences, thus without accidentals. In Eqs. (1), noise photons coming from the pump residual and Raman scattering, typically

linear with the pump power, have not been considered, being negligible in our experimental setup. Singles and coincidence rates can be calculated by multiplying the probabilities in Eqs. (1) by the repetition rate R_p of the pump laser. Together with SFWM, other nonlinear phenomena take place in the waveguide. Two photon absorption (TPA), cross two photon absorption (XTPA), and free carrier absorption (FCA) have to be modeled properly in order to recover the actual generation and transmission efficiency of the pairs. While TPA affects almost only pump photons, XTPA induces losses also to idler and signal photons, occurring between one pump photon and one signal/idler photon.²⁷ In particular, XTPA affects more the idler photon than the signal photon, since the lower energy of the signal photon leads to a reduced probability of the process.²⁸ TPA, XTPA, and FCA play an important role in increasing the losses in the waveguide for both the pump and the generated photons. As a result, the detection probabilities are no longer quadratic with the input pump power.²⁹ A further effect is the nonlinearity of the idler detector. To model the linear and nonlinear losses affecting pump, signal, and idler photons, we solved the differential equations for the pulse propagation involving TPA, FCA, and propagation losses, assuming that the pump power is equally split on the TE0 and TE1 modes.³⁰ According to this modeling, we can rewrite Eqs. (1) as

$$p_{si} \simeq \xi \tilde{P}_p^2 \tilde{\eta}_i \tilde{\eta}_s \eta_{ND} \equiv \tilde{p}_{si}, \quad (2a)$$

$$p_i \simeq (\xi \tilde{P}_p^2 \tilde{\eta}_i + d_i) \eta_{ND} \equiv \tilde{p}_i, \quad (2b)$$

$$p_s \simeq \xi \tilde{P}_p^2 \tilde{\eta}_s + d_s \equiv \tilde{p}_s, \quad (2c)$$

$$p_{acc} \simeq \tilde{p}_i \tilde{p}_s \equiv \tilde{p}_{acc}, \quad (2d)$$

where

$$\tilde{P}_p = \sqrt{\frac{1}{L} \int_0^L P_p^2(z) dz}, \quad (3a)$$

$$\tilde{\eta}_j = \tilde{\eta}_j^{on} \eta_j^{off}, \quad (3b)$$

$$\tilde{\eta}_j^{on} = \frac{1}{L} \int_0^L \eta_j^{on}(z) dz, \quad (3c)$$

where $j = i, s$, L is the waveguide length, $P_p(z)$ is the on-chip pump power along the waveguide, $\eta_j^{on}(z)$ is the transmission efficiency for a photon generated at z along the waveguide accounting only for the linear and nonlinear on-chip losses, η_j^{off} is the transmission efficiency accounting only for the losses occurring off chip (fiber-chip coupling and filtering), and η_{ND} models the nonlinear response of the idler detector. Details about the derivation of Eq. (2) are reported in the [supplementary material](#).

IV. RESULTS

A. Generation probability and heralding efficiency

To monitor the coincidences between signal and idler photons, we used a start-and-stop detection system, using the idler photon as the start trigger and the signal photon as the stop detection.³¹ Coincidences are evaluated within a coincidence window Δt_c . While for the idler channel, the detection rates (both signal and dark counts) are fixed by the detection gate width of the idler detector (1.90 ns), and for the signal channel, the rates depend on the coincidence window used in post-processing. Therefore, given $R_{dc,i} = 620$ cps and

$R_{dc,s} = 2150\text{cps}$, the dark count rates at the idler and signal detectors are

$$d_i = R_{dc,i}/R_p = 7.75 \times 10^{-6} \quad (4)$$

and

$$d_s = 1 - e^{-R_{dc,s}\Delta t_c}, \quad (5)$$

considering a Poisson distribution for the signal noise (SPAD dark counts and UC noise).

In order to fit the measured rates and retrieve the generation probability ξ , we can reduce Eqs. (2) to

$$y_i = \frac{\tilde{p}_i - \eta_{ND} d_i}{\tilde{\eta}_i^{on} \eta_{ND}} = \xi \tilde{p}_p^2 \eta_i^{off} = a_i \tilde{p}_p^2, \quad (6a)$$

$$y_s = \frac{\tilde{p}_s - d_s}{\tilde{\eta}_s^{on}} = \xi \tilde{p}_p^2 \eta_s^{off} = a_s \tilde{p}_p^2, \quad (6b)$$

$$y_{si} = \frac{\tilde{p}_{si}}{\tilde{\eta}_i^{on} \eta_{ND} \tilde{\eta}_s^{on}} = \xi \tilde{p}_p^2 \eta_i^{off} \eta_s^{off} = a_{si} \tilde{p}_p^2, \quad (6c)$$

where $a_i = \xi \eta_i^{off}$, $a_s = \xi \eta_s^{off}$, and $a_{si} = \xi \eta_i^{off} \eta_s^{off}$. y_i , y_s , and y_{si} can be calculated from the measured singles, coincidence, and noise rates as well as from the simulated $\tilde{\eta}_j^{on}$ and the measured η_{ND} (see the [supplementary material](#)). Modeling exactly the nonlinear losses is a non-trivial task, being the nonlinear parameters highly variable with the fabrication process and the geometry used. This particularly affects free carriers whose lifetime is strongly affected by the waveguide cross section³² and the recombination centers on the waveguide surface.³³ Moreover, the nonlinear coefficients of silicon are reported in the literature with large uncertainties.³⁰ Therefore, instead of using published data with large uncertainties, we prefer to estimate the parameters by fitting y_i , y_s , and y_{si} for an input power <0.5 W (i.e., $\tilde{p}_p < 0.4$ W), where the nonlinear losses are not the dominant ones. We use $f(x) = ax^2 + b$ as the fitting function, retrieving a_i , a_s , and a_{si} . In this way, we can evaluate ξ (in units of W^{-2} of peak power) and the off-chip transmissions, resulting in

$$\xi = \frac{a_i a_s}{a_{si}} = (0.70 \pm 0.10) \text{W}^{-2}, \quad (7a)$$

$$\eta_i^{off} = \frac{a_{si}}{a_s} = (2.71 \pm 0.17) \times 10^{-3}, \quad (7b)$$

$$\eta_s^{off} = \frac{a_{si}}{a_i} = (4.00 \pm 0.21) \times 10^{-4}, \quad (7c)$$

where we used $\Delta t_c = 1.1$ ns (3σ bin width) and the uncertainties are evaluated at 1 standard deviation of the fitting coefficients. Details about the nonlinear parameters and propagation losses used in the model are reported in the [supplementary material](#). From these results, we calculate the intrinsic heralding efficiency η_I as³¹

$$\eta_I = \frac{R_{si}^{net}}{(R_i - R_{dc,i}) \eta_s^{off}} = 59 \pm 5\%, \quad (8)$$

where R_{si}^{net} is the measured net coincidence rate and R_i is the measured idler rate. By normalizing for the signal channel losses, η_I allows us to compare different sources only on the basis of their intrinsic properties, getting rid of the specific detector used and of the off-chip transmission losses of the heralded photon (e.g., coupling losses). Our high value comes from the low on-chip signal

losses and the absence of filtering losses to select the signal wavelength. η_I is mainly limited by signal propagation losses, around 3 dB/cm. To also take into account the role of the detection system and off-chip losses, we calculate the Klyshko efficiency,³¹ that is, $\eta_K = R_{si}^{net}/(R_i - R_{dc,i}) = \eta_I \eta_s^{off} = (0.024 \pm 0.002)\%$. This low η_K is mainly due to the upconversion system with a low detection efficiency (~ -20 dB) and a narrow upconversion bandwidth with respect to the signal one (~ -6.5 dB). Even the fiber-chip coupling losses contributes significantly, with $-6.0(5)$ dB per facet.

B. Coincidence to accidental ratio

To quantify the efficiency of coincidence detection, the coincidence-to-accidental ratio (CAR) is used. CAR is analogous to a signal-to-noise ratio comparing the rate of true coincidences with the accidental ones. True coincidences come from simultaneous detection of a signal and an idler belonging to the same pair. Coincidences between signals and idlers belonging to different pairs or coincidences with noise photons or dark counts contribute to the accidentals.^{26,31} The measurement of CAR is carried out with the start-stop coincidence detection described in Sec. IV A. We used the setup in Fig. 1(b) with a single visible SPAD at the output of the UC after removing the beam splitter. In fact, the CAR does not involve the intra-beam correlations. As shown in Fig. 3, the coincidences occur with a temporal delay $\delta t = 0$ ns. The other peaks, spaced with the laser repetition period, are due to accidentals. The zero-delay peak includes also accidental coincidences. Therefore, the CAR is evaluated as

$$\text{CAR} = \frac{\text{coincidence counts}}{\text{accidental counts}} = \frac{N_{si}^{raw} - N_{acc}}{N_{acc}}, \quad (9)$$

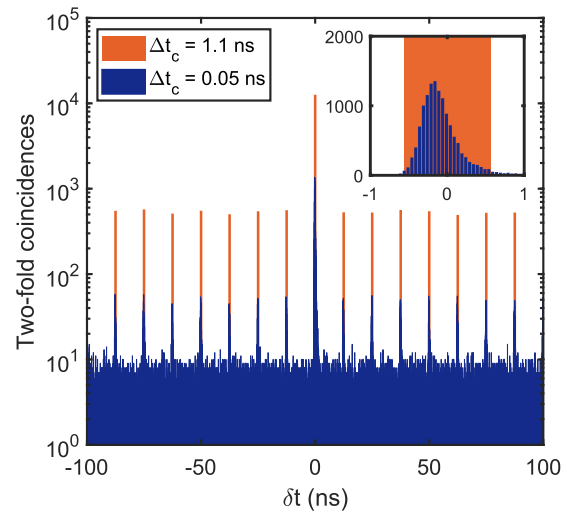


FIG. 3. Twofold coincidences as a function of the delay δt between idler (start) and signal (stop) detections. We collect the events with a coincidence window of 0.05 ns (blue). In post-processing, we use a larger coincidence window of 1.1 ns (orange) in order to take into account the majority of the coincidence events. The coincidence peak is the highest one, placed at $\delta t = 0$ ns. The laser repetition period is clearly visible from the accidental peaks. In the inset, we focus on the zero-delay bin, comparing the coincidence peak shape with the post-processing coincidence window.

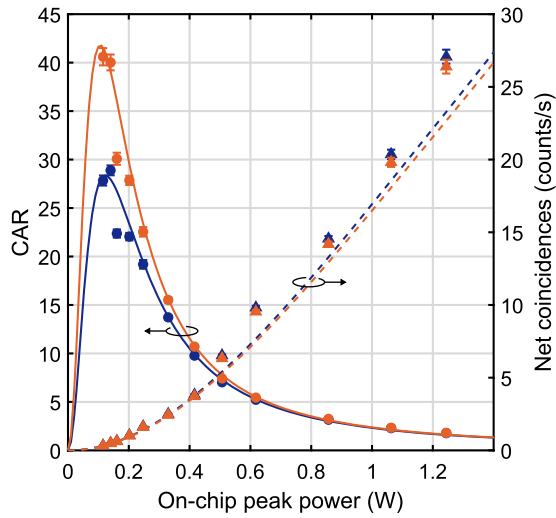


FIG. 4. Measured CAR (circles) and net coincidence rates (triangles) with $\Delta t_c = 1.1$ ns (orange) and $\Delta t_c = 2$ ns (blue). The data are reported vs the on-chip peak pump power. The experimental points are compared with the simulated values for both the CAR (solid lines) and the net coincidence rates (dashed lines). With $\Delta t_c = 1.1$ ns, the CAR is remarkably higher with respect to the 2 ns bin with only a limited reduction in the coincidence rate. The better performance obtained with the smaller Δt_c is due to the lower noise integrated within the coincidence bin.

where N_{si}^{raw} is the total coincidence counts falling in the zero delay bin and N_{acc} is the accidental counts, evaluated as the average over all the accidental peaks. The true coincidences, also called net coincidences, are calculated as $N_{si}^{net} = N_{si}^{raw} - N_{acc}$. Depending on the Δt_c used, the ratio between coincidence and accidentals in the individual bin changes, changing the CAR. In Fig. 4, we report the measured CAR and the corresponding net coincidences as a function of the on-chip peak pump power. The peak power in the plot is the power at the input of the multimode waveguide after fiber-chip coupling losses, and it is not \bar{P}_p . We report the results with a coincidence window of 1.1 ns and 2 ns. With the 1.1 ns window, the CAR is higher with a maximum of 40.4(9) at 115 mW. At this power, the rate of net coincidences is 0.316(3) cps. The net coincidences are almost the same for the two windows, demonstrating that with the larger coincidence window, we are mainly introducing noise rather than the signal. CAR and net coincidences have also been simulated starting from the parameters calculated in Secs. IV A and III. They are reported as solid lines in Fig. 4 and are calculated as²⁶

$$CAR = \frac{\bar{P}_{si}}{\bar{P}_i \bar{P}_s} = \frac{\xi \bar{P}_p^2 \bar{\eta}_i \bar{\eta}_s}{(\xi \bar{P}_p^2 \bar{\eta}_i + d_i) (\xi \bar{P}_p^2 \bar{\eta}_s + d_s)}, \quad (10a)$$

$$N_{si}^{net} = \xi \bar{P}_p^2 \bar{\eta}_i \bar{\eta}_s \eta_{ND} R_p. \quad (10b)$$

The simulated and experimental values of CAR are in agreement with the whole range of pump power used. This agreement demonstrates that the main effects and phenomena involved in the generation process have been properly considered and modeled. The net coincidence rates are in agreement at low power, while at higher power, the nonlinear losses have been overestimated. A perfect agreement would require a precise knowledge of all the nonlinear parameters of the material, as already mentioned in Sec. IV A.

The larger CAR measured here with respect to other works²¹ demonstrates that the overall system, considering both the generation and detection stages, is competitive with respect to solutions already demonstrated on the silicon platform.

C. Heralded $g_h^{(2)}$

To assess the single photon nature of the emission, we measured the heralded $g^{(2)}$, which we indicate as $g_h^{(2)}$. Using the setup in Fig. 1(b), we tuned the delays in order to have the signal detection on one visible SPAD coincident with the idler detection on the InGaAs SPAD. The coincidence between these two detectors, with a coincidence window $\Delta t_c = 2$ ns, was used as the start trigger, while the detection from the remaining visible SPAD, which we will call “delayed signal,” was used as the stop trigger. In this way, we monitored the threefold coincidences as a function of the delay δt between the start and stop events. At the same time, we measured the twofold coincidences between the idler and the delayed signals. We used a coincidence window of 2 ns to monitor the threefold coincidences. The $g_h^{(2)}$ can be given as³¹

$$g_h^{(2)}(\delta t) = \frac{N_{12i}(\delta t)}{N_{1i}(0)N_{2i}(\delta t)} N_i, \quad (11)$$

where 1, 2, i label, respectively, the first signal detector, the second signal detector (that is the delayed signal), and the idler detector. N_{12i} corresponds to the threefold coincidence counts, N_{1i} and N_{2i} are the twofold coincidence counts between the idler and the signal detectors, and N_i corresponds to the idler counts. We can normalize Eq. (11) by N_i and $N_{1i}(0)$ such that

$$g_h^{(2)}(\delta t) = \frac{N_{12i}(\delta t)}{\langle N_{12i}(\delta t \neq 0) \rangle} \frac{\langle N_{2i}(\delta t \neq 0) \rangle}{N_{2i}(\delta t)}, \quad (12)$$

where $\langle N_{12i}(\delta t \neq 0) \rangle$ and $\langle N_{2i}(\delta t \neq 0) \rangle$ are the average of the threefold and twofold coincidences for δt different from zero. If the emission is truly at the single photon level, $g_h^{(2)}(0)$ should be lower than 0.5.³¹ The measured $g_h^{(2)}(0)$ as a function of the on-chip peak pump power is reported in Fig. 5. For an input power of 0.33 W, we measured $g_h^{(2)}(0) = 0.23(8)$, demonstrating the single photon regime of the source. The corresponding $g_h^{(2)}(\delta t)$, calculated as in Eq. (12), is reported in the inset of Fig. 5. We discarded the neighboring bins of the zero delay bin, affected by spurious coincidences due to photon emissions from triggered silicon SPADs.³⁴

To verify the goodness of the modeling introduced in Sec. III, we used the calculated ξ , \bar{P}_p , $\bar{\eta}_i$, and $\bar{\eta}_s$ in Sec. IV A to simulate the expected $g_h^{(2)}(0)$. Considering the general formula for the heralded second-order coherence, we can write

$$g_h^{(2)}(0) = \frac{\bar{P}_{12i} \bar{P}_i}{\bar{P}_{1i} \bar{P}_{2i}}, \quad (13)$$

where \bar{P}_{12i} is the probability per pulse of having a threefold coincidence. To model the experimental results, we have to consider all the possible coincidence events that may involve signal and/or noise detections. By considering all the possible events leading to a

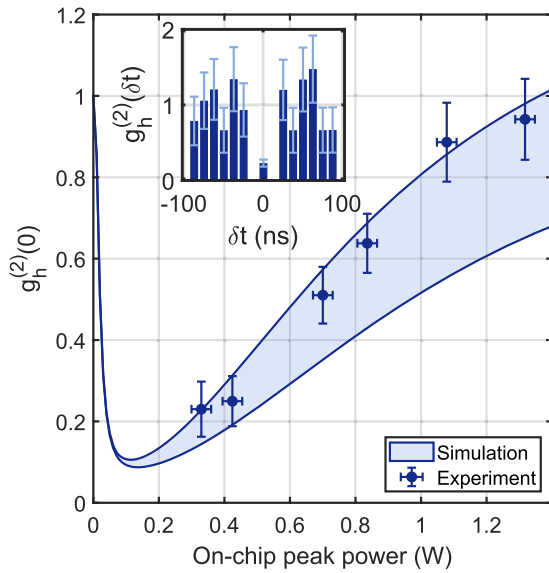


FIG. 5. Comparison between the measured (blue points) and simulated (light blue area) $g_h^{(2)}(0)$ as a function of the on-chip peak power. Measurement for the $g_h^{(2)}(\delta t)$ at an on-chip peak power of 0.33 W is reported in the inset. The bins adjacent to the zero-delayed one have been removed due to the SPAD emitted photons.

threefold coincidence (see the [supplementary material](#)), we can rewrite \tilde{p}_{12i} as

$$\tilde{p}_{12i} = \sum_{n=2}^{\infty} n^2 (n-1) \wp(n) \tilde{\eta}_1 \tilde{\eta}_2 \tilde{\eta}_i \eta_{ND} \quad (14)$$

$$+ \sum_{n=1}^{\infty} n^2 \wp(n) (\tilde{\eta}_1 d_2 + d_1 \tilde{\eta}_2) \tilde{\eta}_i \eta_{ND} \quad (15)$$

$$+ \frac{1}{2} \sum_{n=2}^{\infty} n(n-1) \wp(n) \tilde{\eta}_1 \tilde{\eta}_2 d_i \eta_{ND} \quad (16)$$

$$+ \sum_{n=1}^{\infty} n \wp(n) \tilde{\eta}_1 d_2 d_i \eta_{ND} \quad (17)$$

$$+ \sum_{n=1}^{\infty} n \wp(n) d_1 \tilde{\eta}_2 d_i \eta_{ND} \quad (18)$$

$$+ \sum_{n=1}^{\infty} n \wp(n) d_1 d_2 \tilde{\eta}_i \eta_{ND} \quad (19)$$

$$+ d_1 d_2 d_i \eta_{ND}, \quad (20)$$

where $\wp(n)$ represents the photon number distribution. In Eq. (14), $\tilde{\eta}_i$ is as in Eq. (3c), while $\tilde{\eta}_1$ and $\tilde{\eta}_2$ also take into account the effect of the beam splitter; thus, according to Eq. (3c), they can be written as

$$\tilde{\eta}_1 = \tilde{\eta}_s T_{BS}^2 \eta_{BS}, \quad (21a)$$

$$\tilde{\eta}_2 = \tilde{\eta}_s R_{BS}^2 \eta_{BS}, \quad (21b)$$

where T_{BS} and R_{BS} represent the transmission and reflection coefficients of the beam splitter, respectively, $T_{BS}^2 + R_{BS}^2 = 1$, and η_{BS} is modeling the losses of the beam splitter. In our case, $T_{BS}^2 = R_{BS}^2 = 0.5$

and $\eta_{BS} = 1$. In Eqs. (21), we are assuming the same detection efficiency for the two visible SPADs. Considering all the events leading to a twofold coincidence, we can rewrite \tilde{p}_{1i} and \tilde{p}_{2i} as

$$\tilde{p}_{ki} = \sum_{n=1}^{\infty} n^2 \wp(n) \tilde{\eta}_k \tilde{\eta}_i \eta_{ND} \quad (22)$$

$$+ \sum_{n=1}^{\infty} n \wp(n) (\tilde{\eta}_k d_i + d_k \tilde{\eta}_i) \eta_{ND} \quad (23)$$

$$+ d_k d_i \eta_{ND}, \quad (24)$$

with $k = 1, 2$. In Eqs. (14) and (22), we are neglecting events with more than one photon reaching the same detector, being unlikely with the involved transmission efficiencies (i.e., $\tilde{\eta}_i$, $\tilde{\eta}_1$, and $\tilde{\eta}_2$ are all $\ll 1$). We are also neglecting events where photon detections and dark count detections occur simultaneously on the same detector. The photon number distribution of a squeezed source ranges between a Poissonian (infinite modes' emission) and a thermal (single mode emission) distribution.^{31,35} We solved Eqs. (14) and (22) for the Poissonian emission,

$$\wp(n) = \frac{\mu^n}{n!} e^{-\mu}, \quad (25)$$

and for the thermal emission,

$$\wp(n) = \frac{\mu^n}{(1 + \mu)^{n+1}}, \quad (26)$$

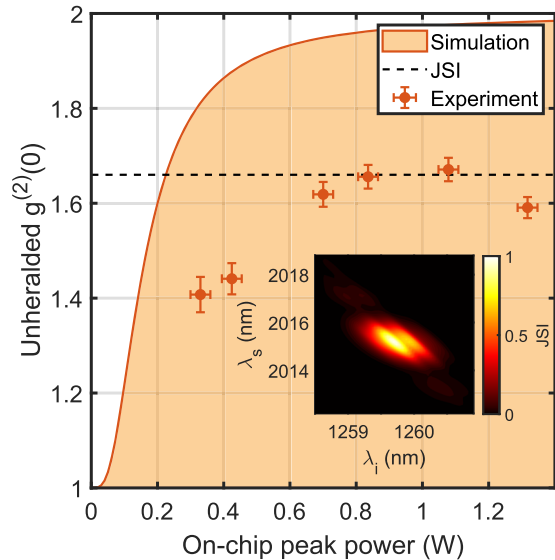


FIG. 6. The measured unheralded $g^{(2)}(0)$ (orange dots) is reported as a function of the on-chip peak power. We report in the inset the simulated JSI from which we calculated the expected $g^{(2)}$ (dashed black line), which is compatible with the experiment. The measured points fall within the simulated values (light orange area), upper bounded by a source with thermal emission statistics and lower bounded by a source with Poissonian emission statistics (constant $g^{(2)} = 1$). The asymmetry in the JSI is due to the pump spectrum (see the [supplementary material](#)).

TABLE I. Comparison with state-of-the-art MIR heralded sources.

Platform	Process	Generation probability (W^{-2})	CAR max	CAR at $N_{si}^{net} \sim 1$ Hz	$g_h^{(2)}(0)$	η_I (%)	References
Mg:PPLN	SPDC	...	180 ± 50	19
SOI	Intra-modal SFWM	0.28	25.7 ± 1.1	25.7 ± 1.1	...	5	21
SOI	Inter-modal SFWM	0.70 ± 0.10	40.4 ± 0.9	27.9 ± 0.5	0.23 ± 0.08	59 ± 5	This work

where μ is the average number of pair per pulse. Equations (25) and (26) define a lower and an upper boundary for $g_{h, \text{sim}}^{(2)}$. In computing $g_h^{(2)}$, we calculated μ as $\mu = \xi \bar{P}_p^2$ and we measured the noise affecting the three channels. d_i is the same of the CAR measurements, $d_1 = 2.30 \times 10^{-6}$ and $d_2 = 2.32 \times 10^{-6}$. We simulated an area for the expected value of the $g_h^{(2)}(0)$, which is upper bounded by the thermal case and lower bounded by the Poissonian case. The simulation is reported in Fig. 5. The measured $g_h^{(2)}$ is compatible with the simulated values, confirming the reliability of the modeling. We want to stress that in this case we are not performing a fit of the measured $g_h^{(2)}$ and that the experiment and the simulation are completely independent. The experimental points in Fig. 5 are closer to the upper bound rather than to the lower one, suggesting an emission statistics closer to the thermal one. This is compatible with the unheralded $g^{(2)}$ of the signal beam,³¹ measured in Fig. 6 as a function of the pump power. The unheralded $g^{(2)}$ results to be 1.67(2) at a power of 1.08 W, compatible with the simulated value of 1.66 (dashed line) calculated from the simulated joint spectral intensity (JSI).^{31,36} The measured $g^{(2)}$ demonstrates that the source is closer to a thermal emission, justifying the experimental $g_h^{(2)}$. In Fig. 6, we also report the simulated values for a source whose statistics is between the thermal (upper bound) and the Poissonian one (lower bound). At low powers, the dark counts dominate, and in both cases, the $g^{(2)}$ goes to 1. At high powers, the $g^{(2)}$ asymptotically increases to its actual value. In this way, we explain the power-dependent behavior of the experimental data. Further details about the measurement and simulation of $g^{(2)}$ are reported in the [supplementary material](#).

V. CONCLUSIONS

In this work, we demonstrated a heralded single-photon source beyond $2 \mu\text{m}$ based on inter-modal SFWM on a silicon chip. This source has two main peculiarities: the discrete band generation and the large detuning between the signal and idler photons. The discrete band generation removes the need for tight filtering to select idler and signal wavelengths, and the generated photons experience a higher transmission with respect to standard continuous band sources, witnessed by the high experimental $\eta_I = 59(5)\%$. The large detuning has two advantages: (1) It enables an easier pump and nonlinear noise rejection. (2) It allows us to generate the herald photon in the NIR, benefiting from an efficient detection technology. As a last advantage, this heralded source based on inter-modal SFWM requires a common C-band pump laser, easier to be integrated and operated on a silicon chip. We performed a complete characterization of the source. We demonstrated the sub-Poissonian statistics of the source by measuring $g_h^{(2)}(0) = 0.23(8)$. We characterized the CAR, finding a maximum value of $40.4(9)$,

and the generation probability per pulse with a measured value of $0.70(10) \text{ W}^{-2}$. These performances are competitive with other reported silicon sources of MIR photons (Table I) demonstrating the promising perspectives of inter-modal SFWM for bright and efficient sources of correlated photons beyond $2 \mu\text{m}$. The source can be significantly improved by reducing the propagation losses and optimizing the matching between the signal and upconverter bandwidths. With this work, we demonstrate a new approach to MIR quantum photonics, providing a high-quality source of quantum light beyond $2 \mu\text{m}$ without the need for MIR technologies. This result paves the way toward low cost, efficient, and integrated solutions for quantum photonics beyond $2 \mu\text{m}$, offering new opportunities to the developing field of MIR photonics.

SUPPLEMENTARY MATERIAL

See the [supplementary material](#) for further details about the experimental setup, the measurements, and the theoretical calculations.

ACKNOWLEDGMENTS

This work was partially supported by grants from Q@TN provided by the Provincia Autonoma di Trento. The authors acknowledge HC Photonics, which fabricated the PPLN crystals used for the upconversion system. S.S. thanks Dr. Massimo Borghi for fruitful discussions and precious suggestions, and Mr. Davide Rizzotti for his careful revision of the manuscript.

AUTHOR DECLARATIONS

Conflict of Interest

The authors declare no conflicts of interest.

DATA AVAILABILITY

The data that support the findings of this study are available from the corresponding author upon reasonable request.

REFERENCES

- Y. Su *et al.*, "10 Gbps DPSK transmission over free-space link in the mid-infrared," *Opt. Express* **26**, 34515–34528 (2018).
- P. Weibring, H. Edner, and S. Svanberg, "Versatile mobile lidar system for environmental monitoring," *Appl. Opt.* **42**, 3583–3594 (2003).
- A. Fix, L. Högstedt, C. Pedersen, P. Tidemand-Lichtenberg, and M. Wirth, "Upconversion-based lidar measurements of atmospheric CO_2 ," in *Optics and Photonics for Energy and the Environment* (Optical Society of America, 2016), paper EM4A.5.
- C. L. Evans *et al.*, "Chemically-selective imaging of brain structures with CARS microscopy," *Opt. Express* **15**, 12076–12087 (2007).

- ⁵G. Bellisola and C. Sorio, "Infrared spectroscopy and microscopy in cancer research and diagnosis," *Am. J. Cancer Res.* **2**, 1 (2012).
- ⁶K. Potter, L. H. Kidder, I. W. Levin, E. N. Lewis, and R. G. S. Spencer, "Imaging of collagen and proteoglycan in cartilage sections using Fourier transform infrared spectral imaging," *Arthritis Rheum.* **44**, 846–855 (2001).
- ⁷L. M. Miller, M. W. Bourassa, and R. J. Smith, "FTIR spectroscopic imaging of protein aggregation in living cells," *Biochim. Biophys. Acta, Biomembr.* **1828**, 2339–2346 (2013).
- ⁸D. Popa and F. Udreă, "Towards integrated mid-infrared gas sensors," *Sensors* **19**, 2076 (2019).
- ⁹C. R. Petersen *et al.*, "Mid-infrared supercontinuum covering the 1.4–13.3 μm molecular fingerprint region using ultra-high NA chalcogenide step-index fibre," *Nat. Photonics* **8**, 830 (2014).
- ¹⁰M. Vainio and L. Halonen, "Mid-infrared optical parametric oscillators and frequency combs for molecular spectroscopy," *Phys. Chem. Chem. Phys.* **18**, 4266–4294 (2016).
- ¹¹R. Ghorbani and F. M. Schmidt, "Real-time breath gas analysis of CO and CO₂ using an EC-QCL," *Appl. Phys. B* **123**, 144 (2017).
- ¹²G. Brida, M. Genovese, and I. Ruo Berchera, "Experimental realization of sub-shot-noise quantum imaging," *Nat. Photonics* **4**, 227 (2010).
- ¹³R. Whittaker *et al.*, "Absorption spectroscopy at the ultimate quantum limit from single-photon states," *New J. Phys.* **19**, 023013 (2017).
- ¹⁴T. B. Pittman, Y. H. Shih, D. V. Strekalov, and A. V. Sergienko, "Optical imaging by means of two-photon quantum entanglement," *Phys. Rev. A* **52**, R3429 (1995).
- ¹⁵P. A. Morris, R. S. Aspdén, J. E. Bell, R. W. Boyd, and M. J. Padgett, "Imaging with a small number of photons," *Nat. Commun.* **6**, 5913 (2015).
- ¹⁶G. B. Lemos *et al.*, "Quantum imaging with undetected photons," *Nature* **512**, 409–412 (2014).
- ¹⁷D. A. Kalashnikov, A. V. Paterova, S. P. Kulik, and L. A. Krivitsky, "Infrared spectroscopy with visible light," *Nat. Photonics* **10**, 98 (2016).
- ¹⁸P. Vergyris, C. Babin, R. Nold, E. Gouzien, H. Herrmann, C. Silberhorn, O. Alibart, S. Tanzilli, and F. Kaiser, "Two-photon phase-sensing with single-photon detection," *Appl. Phys. Lett.* **117**, 024001 (2020).
- ¹⁹S. Prabhakar, T. Shields, A. C. Dada, M. Ebrahim, G. G. Taylor, D. Morozov, K. Erotokritou, S. Miki, M. Yabuno, H. Terai *et al.*, "Two-photon quantum interference and entanglement at 2.1 μm ," *Sci. Adv.* **6**, eaay5195 (2020).
- ²⁰D. J. Lockwood and L. Pavesi, *Silicon Photonics II: Components and Integration* (Springer Science & Business Media, 2010), Vol. 119.
- ²¹L. M. Rosenfeld, D. A. Sulway, G. F. Sinclair, V. Anant, M. G. Thompson, J. G. Rarity, and J. W. Silverstone, "Mid-infrared quantum optics in silicon," *Opt. Express* **28**, 37092–37102 (2020).
- ²²S. Signorini *et al.*, "Intermodal four-wave mixing in silicon waveguides," *Photonics Res.* **6**, 805–814 (2018).
- ²³S. Signorini *et al.*, "Silicon photonics chip for inter-modal four wave mixing on a broad wavelength range," *Front. Phys.* **7**, 128 (2019).
- ²⁴M. Mancinelli *et al.*, "Mid-infrared coincidence measurements on twin photons at room temperature," *Nat. Commun.* **8**, 15184 (2017).
- ²⁵S. Paesani, M. Borghi, S. Signorini, A. Maïnos, L. Pavesi, and A. Laing, "Near-ideal spontaneous photon sources in silicon quantum photonics," *Nat. Commun.* **11**, 1–6 (2020).
- ²⁶K.-i. Harada, H. Takesue, H. Fukuda, T. Tsuchizawa, T. Watanabe, K. Yamada, Y. Tokura, and S.-i. Itabashi, "Frequency and polarization characteristics of correlated photon-pair generation using a silicon wire waveguide," *IEEE J. Sel. Top. Quantum Electron.* **16**, 325–331 (2009).
- ²⁷C. A. Husko, A. S. Clark, M. J. Collins, A. De Rossi, S. Combrié, G. Lehoucq, I. H. Rey, T. F. Krauss, C. Xiong, and B. J. Eggleton, "Multi-photon absorption limits to heralded single photon sources," *Sci. Rep.* **3**, 3087 (2013).
- ²⁸N. Poulvellarie, C. Ciret, B. Kuyken, F. Leo, and S.-P. Gorza, "Highly nondegenerate two-photon absorption in silicon wire waveguides," *Phys. Rev. Appl.* **10**, 024033 (2018).
- ²⁹R. W. Boyd, *Nonlinear Optics* (Academic Press, 2019).
- ³⁰M. Borghi, C. Castellan, S. Signorini, A. Trenti, and L. Pavesi, "Nonlinear silicon photonics," *J. Opt.* **19**, 093002 (2017).
- ³¹S. Signorini and L. Pavesi, "On-chip heralded single photon sources," *AVS Quantum Sci.* **2**, 041701 (2020).
- ³²D. Dimitropoulos, R. Jhaveri, R. Claps, J. C. S. Woo, and B. Jalali, "Lifetime of photogenerated carriers in silicon-on-insulator rib waveguides," *Appl. Phys. Lett.* **86**, 071115 (2005).
- ³³J. Van Campenhout, W. M. J. Green, X. Liu, S. Assefa, R. M. Osgood, and Y. A. Vlasov, "Silicon-nitride surface passivation of submicrometer silicon waveguides for low-power optical switches," *Opt. Lett.* **34**, 1534–1536 (2009).
- ³⁴C. Kurtsiefer, P. Zarda, S. Mayer, and H. Weinfurter, "The breakdown flash of silicon avalanche photodiodes-back door for eavesdropper attacks?," *J. Mod. Opt.* **48**, 2039–2047 (2001).
- ³⁵H. Takesue and K. Shimizu, "Effects of multiple pairs on visibility measurements of entangled photons generated by spontaneous parametric processes," *Opt. Commun.* **283**, 276–287 (2010).
- ³⁶M. Borghi, "Phase-resolved joint spectra tomography of a ring resonator photon pair source using a silicon photonic chip," *Opt. Express* **28**, 7442–7462 (2020).